nature chemistry

Article

https://doi.org/10.1038/s41557-023-01380-1

Cooperative H_2 activation at a nickel(0)–olefin centre

Received: 6 February 2023

Accepted: 23 October 2023

Published online: 5 December 2023

Check for updates

María L. G. Sansores-Paredes [1], Martin Lutz [2] & Marc-Etienne Moret [1]

Catalytic olefin hydrogenation is ubiquitous in organic synthesis. In most proposed homogeneous catalytic cycles, reactive M–H bonds are generated either by oxidative addition of H_2 to a metal centre or by deprotonation of a non-classical metal dihydrogen (M–H_2) intermediate. Here we provide evidence for an alternative H_2-activation mechanism that instead involves direct ligand-to-ligand hydrogen transfer (LLHT) from a metal-bound H_2 molecule to a metal-coordinated olefin. An unusual pincer ligand that features two phosphine ligands and a central olefin supports the formation of a non-classical Ni–H_2 complex and the Ni(alkyl)(hydrido) product of LLHT, in rapid equilibrium with dissolved H_2. The usefulness of this cooperative H_2-activation mechanism for catalysis is demonstrated in the semihydrogenation of diphenylacetylene. Experimental and computational mechanistic investigations support the central role of LLHT for H_2 activation and catalytic semihydrogenation. The product distribution obtained is largely determined by the competition between (*E*)–(Z) isomerization and catalyst degradation by self-hydrogenation.

Catalytic hydrogenation reactions, which add molecular H_2 to an organic molecule[1–3], are atom economic, cost-effective and therefore attractive from an environmental point of view[2–6]. This motivates sustained efforts to understand the activation of H_2 by transition metal (TM) catalysts. Classically, reduced TMs are thought to activate the H–H bond via a combination of σ-donation from H_2 to the metal and π-backdonation from the metal *d*-electrons to the σ^*(H–H) orbital (Fig. 1a). Strong orbital interactions cleave the H–H bond to form a metal dihydride (oxidative addition, Fig. 1b)[3,4,6–8], whereas weaker ones result in non-classical dihydrogen complexes preserving H–H bonding[8–10].

Activation of H_2 is generally more challenging with 3*d* metals than with 4*d* or 5*d* metals because they form weaker M–H bonds. Nevertheless, hydrogenations catalysed by 3*d* metals are attracting considerable interest due to their abundance, low cost and generally lower toxicity[11]. Bifunctional catalysts that involve ligands actively participating in the cleavage of the H–H bond[11–14] play a central role in this transition (Fig. 1c)[11–13,15–19]. Prominent examples include ligand-centred deprotonation of the H_2 molecule to generate a hydride without formally oxidizing the metal[11,13,20–23], which can be coupled to the reversible aromatization/dearomatization of a N-heterocyclic ligand[17]. Conversely, Lewis acids have been recently shown to accept a formal hydride from H_2 to form a M–H bond, with concomitant oxidation of the metal[11,13,20–23]. Furthermore, metal–metal proximity can assist in polarizing and cleaving the H–H bond in bimetallic catalysts[13,24].

Against this backdrop, we hypothesized that a π-bound olefin could be used for cooperative H_2 activation (Fig. 1d). Since the discovery of non-classical H_2 complexes by Kubas and co-workers[25], a long-standing question has been whether hydrogen atoms can be transferred to unsaturated substrates without prior H–H cleavage. Supporting evidence came (among others) from kinetic studies on olefin hydrogenation involving a diruthenium–H_2 intermediate and parahydrogen-induced polarization experiments on photoinduced hydrogenation mediated by transient [$Mo(CO)_3(H_2)$(olefin)][3,26–31]. Some olefin diphosphine pincer ligands have been used to characterize details of TM–olefin chemistry, including an unusual reversible β-insertion of an olefin in a M–H bond that showed that hydride migration can occur between ligands occupying *trans* positions[15,32–39].

[1]Organic Chemistry and Catalysis, Institute for Sustainable and Circular Chemistry, Faculty of Science, Utrecht University, Utrecht, the Netherlands. [2]Structural Biochemistry, Bijvoet Centre for Biomolecular Research, Faculty of Science, Utrecht University, Utrecht, the Netherlands. e-mail: m.moret@uu.nl

https://doi.org/10.1038/s41557-023-01380-1

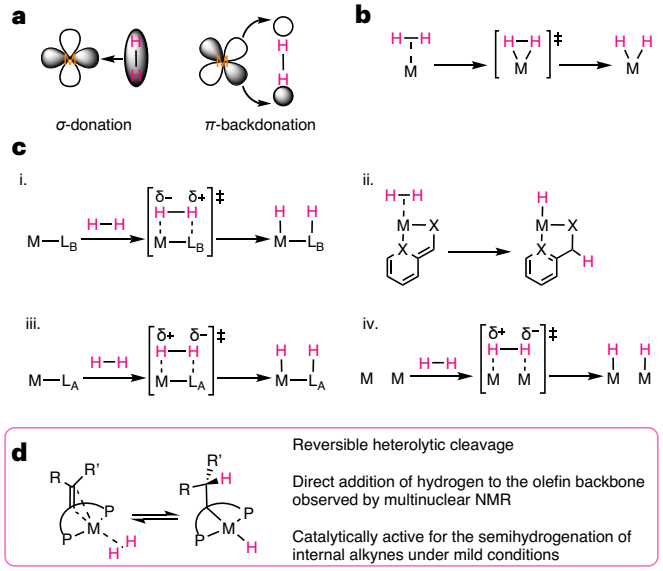

Fig. 1 | Strategies for H_2 activation in homogeneous catalysis. a, Orbital interactions involved in the bonding of H_2 with transition metals. **b**, Classical single-site activation of hydrogen by transition metals. **c**, Cooperative mechanisms: (i) interaction with a metal centre and a Lewis base (L_B) polarizes the H–H molecule, which is ultimately deprotonated to form a metal hydride; (ii) aromatization/dearomatization: formation of an aromatic system drives H–H bond activation; (iii) interaction with a reduced metal centre and a Lewis acid (L_A) polarizes the H–H molecule, which ultimately protonates the metal centre and transfers a hydride equivalent to the Lewis acid; (iv) interaction with two metal centres results in a bimetallic oxidative addition. **d**, Cooperative activation with a coordinated olefin (this work).

The thermodynamic resistance to β-hydride elimination from alkyl complexes of 3*d* metals such as Ni(II) further suggested that hydride transfer to a coordinated olefin could drive cooperative H_2 activation[40]. Further hypothesizing that the hydricity of the resulting Ni–H bond may be enhanced by the *trans* alkyl carbon[41,42], we set out to investigate the reactivity of Ni(0) complexes of a PC=CP pincer ligand with H_2.

We show that an olefin pincer ligand framework allows for the observation of both a non-classical Ni–(H_2) intermediate and the corresponding alkyl(hydrido) activation product, both in rapid equilibrium with dissolved H_2. Experiments and DFT calculations support a direct ligand-to-ligand hydrogen transfer (LLHT) mechanism without a dihydride intermediate[43–46]. The catalytic relevance of this cooperative mechanism is demonstrated in the selective semihydrogenation of diphenylacetylene to *Z*-stilbene under mild conditions, with a comparable performance to recently disclosed, nickel-based systems[5,47–51].

Results and discussion

Hydrogen activation

We had previously reported the synthesis of a Ni(0)–N_2 complex of the bulky olefin pincer ligand $^{Ph}bppe^{H,CH^pTol_2}$ (bppe = 1,1-bis(2-phosphinophenyl)ethylene)[52]. Although this complex crystallizes as the N_2-bridged dimer [($^{Ph}bppe^{H,CH^pTol_2}$)Ni]$_2$(μ-N_2) (**1**^{dimer}), an intense IR absorption at 2,150 cm^{-1} indicates the presence of the mononuclear form ($^{Ph}bppe^{H,CH^pTol_2}$)Ni(N_2) (**1**) in toluene solution under N_2 (Fig. 2a and Supplementary Section 2)[52,53]. Monitoring by NMR spectroscopy showed that the N_2 co-ligand is easily displaced by addition of H_2 (1 atm) to such a solution. At 25 °C, both $^{31}P\{^1H\}$ and ^{1}H-NMR spectra displayed broad signals. The absence of a ^{1}H-NMR signal for dissolved H_2 suggests exchange processes involving H_2 (ref. 23). Cooling the solution down to −40 °C caused the reappearance of the H_2 signal at 4.54 ppm and decoalescence of both $^{31}P\{^1H\}$ and ^{1}H-NMR spectra to sharp lines, allowing for the identification of three nickel-containing species (Fig. 2a, and Supplementary Sections 1.1 and 1.2).

Two minor species are observed: the first is a residual amount of the known N_2 complex **1** as shown by two $^{31}P\{^1H\}$-NMR doublets at 11.3 and 28.2 ppm ($J_{P,P}$ = 53 Hz), and an ^{1}H-NMR signal at δ = 4.75 ppm corresponding to the olefinic CH group. The two phosphorus atoms in **1** are chemically inequivalent because of the unsymmetrical substitution of the central double bond. The second minor species displays similar characteristics: two $^{31}P\{^1H\}$-NMR doublets at 15.5 and 32.8 ppm ($J_{P,P}$ = 58 Hz) and an olefinic ^{1}H signal at δ = 4.35 ppm (Supplementary Section 1.1). It also features a broad ^{1}H-NMR signal at −2.1 ppm, which suggests its assignment as the non-classical-H_2/olefin species **2**. This was unambiguously confirmed by repeating the experiment under an HD atmosphere: a triplet signal (Fig. 2b) with $^1J_{H,D}$ = 34 Hz corresponds to a H–H bond length of 0.86 Å according to the Heinekey empirical relationship[2,4,54,55], in good agreement with previous reports for Ni(0)–H_2 complexes[2,4,20,23,48,54–58].

The major species was assigned as the alkyl(hydrido) Ni(II) complex **3** resulting from cooperative H_2 addition concomitantly forming new C–H and Ni–H bonds. A single, slightly broadened $^{31}P\{^1H\}$ signal at 40.6 ppm (Supplementary Section 1.1) indicates two chemically equivalent phosphorus atoms. A triplet ^{1}H-NMR signal at δ = −14.3 ppm ($^2J_{H,P}$ = 54 Hz) is evidence of a Ni–H bond with coupling to two equivalent phosphorus nuclei (Fig. 2b). Slightly broadened signals corresponding to the alkyl CH_2 (δ = 3.1 ppm) and CH (δ = 3.8 ppm) groups bolster the assignment of **3**, which was further corroborated by a ^{13}C attached proton test (APT) and ^{1}H–^{1}H correlated spectroscopy (COSY) experiments (Supplementary Section 1.1). An ^{1}H–^{1}H exchange spectroscopy experiment at −40 °C demonstrates rapid chemical exchange between complex **2**, complex **3** and dissolved H_2 (Fig. 2c). Namely, cross-peaks were observed between the Ni–H signal of **3** at −14.3 ppm and free H_2 (4.54 ppm), the Ni–H_2 signal of **2** at −2.1 ppm, and the CH_2 signal of **3**. Exchange between free and nickel-bound H_2 was also observed.

Well-characterized Ni(0)–H_2 complexes were hitherto limited to those incorporating either an additional *σ*-ligand[58] or a *σ*-acceptor ligand—the latter assisting coordination by lowering the energy of the *σ*-antibonding *d*-orbital[2,4,6,20,23,53,57,59–61] and, in some cases, allowing H_2 deprotonation to form strongly hydridic d^{10} hydrides[62,63]. The observation of complex **2** demonstrates that a single *π*-acidic olefin ligand is sufficient to stabilize a H_2 complex of a d^{10} metal and can cooperatively generate an active hydride without the need for full oxidative addition to a dihydride intermediate.

Density functional theory calculations performed on a slightly truncated model support a concerted activation pathway (Fig. 3a). Slightly endergonic (7.5 kcal mol^{-1}) exchange of N_2 for H_2 to form complex **2** is followed by a concerted transition state for H_2 activation (**TS1**, 20.7 kcal mol^{-1}) that is directly connected to structure **3a**, a higher-energy rotamer of the final alkyl(hydrido)nickel complex **3**. The predicted exergonicity of −8.4 kcal mol^{-1} from **2** to **3** is consistent with **3** being the main species in solution, but the presence of **2** in measurable concentration suggests that this energy difference is slightly overestimated. A putative nickel–dihydride structure was also located at 14.6 kcal mol^{-1}; however, forming this structure requires the olefin to leave the coordination sphere of nickel and no transition state connecting it to the products could be located (Supplementary Section 4.4).

The optimized structure of complex **2** (Fig. 3b) confirms a genuine H_2 complex with an H–H bond length of 0.836 Å, in good agreement with the experimental estimation (0.86 Å)[2,4,54,55]. The C=C backbone is slightly elongated (1.427 Å) and pyramidalized (sum of valence angles of 354.4° and 351.6° around C10 and C41, respectively) as a consequence of *π*-backdonation from the nickel centre. The H–H vector is out of the nickel–olefin plane, suggesting that both ligands are receiving *π*-backdonation from different *d*-orbitals. In **TS1** (Fig. 3c), both carbon atoms of the olefin fragment remain coordinated maintain close to sp^2 hybridization with a bond length of 1.450 Å, and angle sums of 348.0°

https://doi.org/10.1038/s41557-023-01380-1

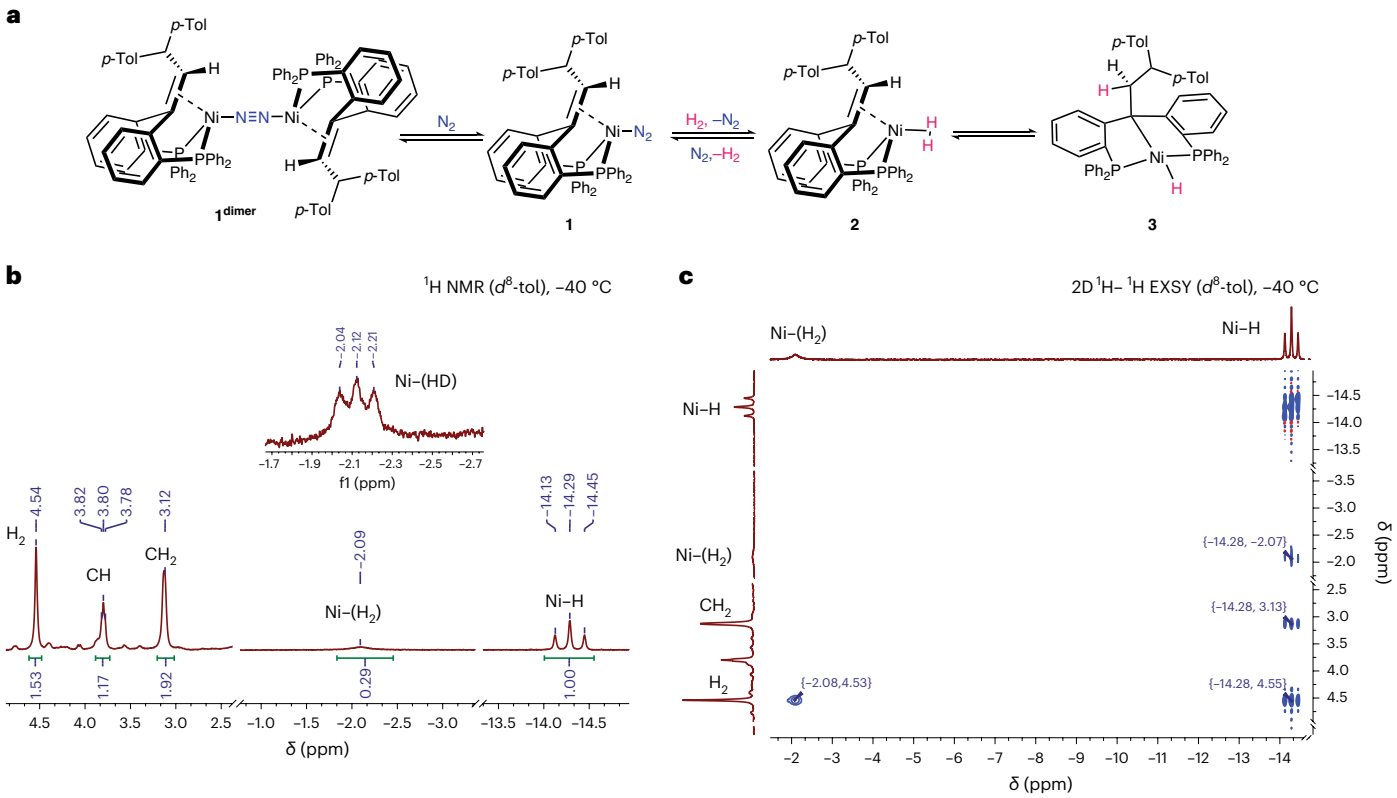

Fig. 2 | Cooperative activation of H_2 by a nickel/olefin complex. a, Equilibrium reaction among complex $\mathbf{1}^{dimer}$, **1**, **2** and **3** under an H_2 atmosphere. Fast exchange of N_2 by H_2 leads to the formation of the Ni–H_2 complex **2**, from which cooperative activation of H_2 by the olefin backbone yields alkyl(hydrido) Ni(II) complex **3**. **b**, Extract of a ^{1}H-NMR spectrum at −40 °C in d^8-tol of the equilibrium mixture of **1**, **2** and **3** under H_2, showing the diagnostic features for the major species **3** and a broad feature corresponding to the Ni–H_2 complex **2**. The inset is an extract of a ^{1}H{^{31}P}-NMR at −40 °C in d^8-tol under HD showing the Ni–(HD) peak of **2** with a characteristic triplet multiplicity arising from H–D coupling (see Supplementary Section 2.1). **c**, Extract of the 2D ^{1}H–^{1}H EXSY spectrum at −40 °C in d^8-tol of the equilibrium among **1**, **2** and **3** (see Supplementary Section 2.2). Cross peaks indicate rapid chemical exchange between free H_2, coordinated H_2 in **2**, and the CH_2 and Ni–H positions in **3**.

and 352.8°. By contrast, the H–H bond is cleaved (1.536 Å) and both the Ni–H95 (1.456 Å) and Ni–H96 (1.480 Å) distances have become shorter than in **2**. These structural observations collectively suggest that the transition state has a strong olefin/dihydride character, with the metal already being oxidized to Ni(II).

The quantum theory of atoms in molecules (QTAIM) has proven a useful framework to characterize complex bonding situations and transition states[64,65]. Relying on topological analysis of the electron density of a molecule (or a transition state), it analyses chemical bonds as ridges of electron density (bond paths) connecting two atoms (maxima of the electron density) via a stationary point referred to as the bond critical point (BCP). Complex **2** (Fig. 3b) exhibits ionic BCPs characterized by a positive Laplacian of the electron density ($\nabla^2\rho$, expressed in atomic units) for both Ni–C bonds (C41–Ni1 $\nabla^2\rho = 0.250$, C10–Ni1 $\nabla^2\rho = 0.237$) and a covalent BCP ($\nabla^2\rho < 0$) for the C41–C10 bond ($\nabla^2\rho = -0.753$), as typical for metal–olefin complexes. A bond path originating from nickel points first towards the centre of the H–H bond, but curves towards H95 after an ionic BCP ($\nabla^2\rho = 0.395$), which is evidence of a bond catastrophe (that is, the BCP between Ni–H96 and the ring critical point (RCP) for Ni–H95–H96 have coalesced), as has been observed for other dihydrogen complexes[66,67]. In **TS1** (Fig. 3c), the C=C backbone displays similar BCPs to complex **2** (C41–Ni1: $\nabla^2\rho = 0.259$; C10–Ni1: $\nabla^2\rho = 0.239$; C41–C10 $\nabla^2\rho = -0.708$). The H–H bond is broken, but both atoms display slightly ionic Ni–H bonds (Ni–H95: $\nabla^2\rho = 0.121$; Ni–H96 $\nabla^2\rho = 0.092$) with a substantial increase in covalency with respect to the Ni–H_2 interaction in complex **2**. A BCP between C41 and H95 located in the ionic area ($\nabla^2\rho = 0.010$) corresponds to the barely formed C–H bond. These observations support the description of **TS1** as resembling an olefin-coordinated Ni(II) dihydride (NiH_2) complex.

This description of **TS1** is consistent with a LLHT step consisting of a concerted hydrogen atom transfer between two ligands (the H_2 molecule and the olefin) with concomitant oxidation of nickel[43,44]. This mechanism was first described in nickel-catalysed hydrofluoroarylation of alkynes: a fluoroarene first coordinates in an η^2(C,H) fashion to an η^2(C,C)-alkyne nickel(0) complex to then transfer a hydrogen atom to the alkyne without a hydride intermediate. This mechanism is favoured for smaller metal centres such as nickel, and LLHT steps have also been invoked for C–H bond activation reactions at nickel/olefin complexes[43–46,68–70].

Catalytic activity in the semihydrogenation of alkynes

Having found that complex **1** activates H_2 efficiently and reversibly via LLHT, we investigated whether this elementary step can be harvested for catalytic hydrogenation. Inspired by recent progress in the nickel-catalysed semihydrogenation of alkynes[5,47–49], we chose the hydrogenation of diphenylacetylene as model reaction. With 10 mol% catalyst at 70 °C in d^8-toluene (d^8-tol) under 4.6 atm H_2 after 22 h, *E*-stilbene (80%) and *Z*-stilbene (12%) were detected with a small amount of overhydrogenation to diphenylethane (8%) (Table 1). The solution remained visually homogeneous throughout the reaction, and a mercury drop did not hinder catalysis, suggesting a homogeneous system. Gradually decreasing the catalyst loading to 1 mol% still allows full conversion to mostly stilbenes, albeit with a longer reaction time

https://doi.org/10.1038/s41557-023-01380-1

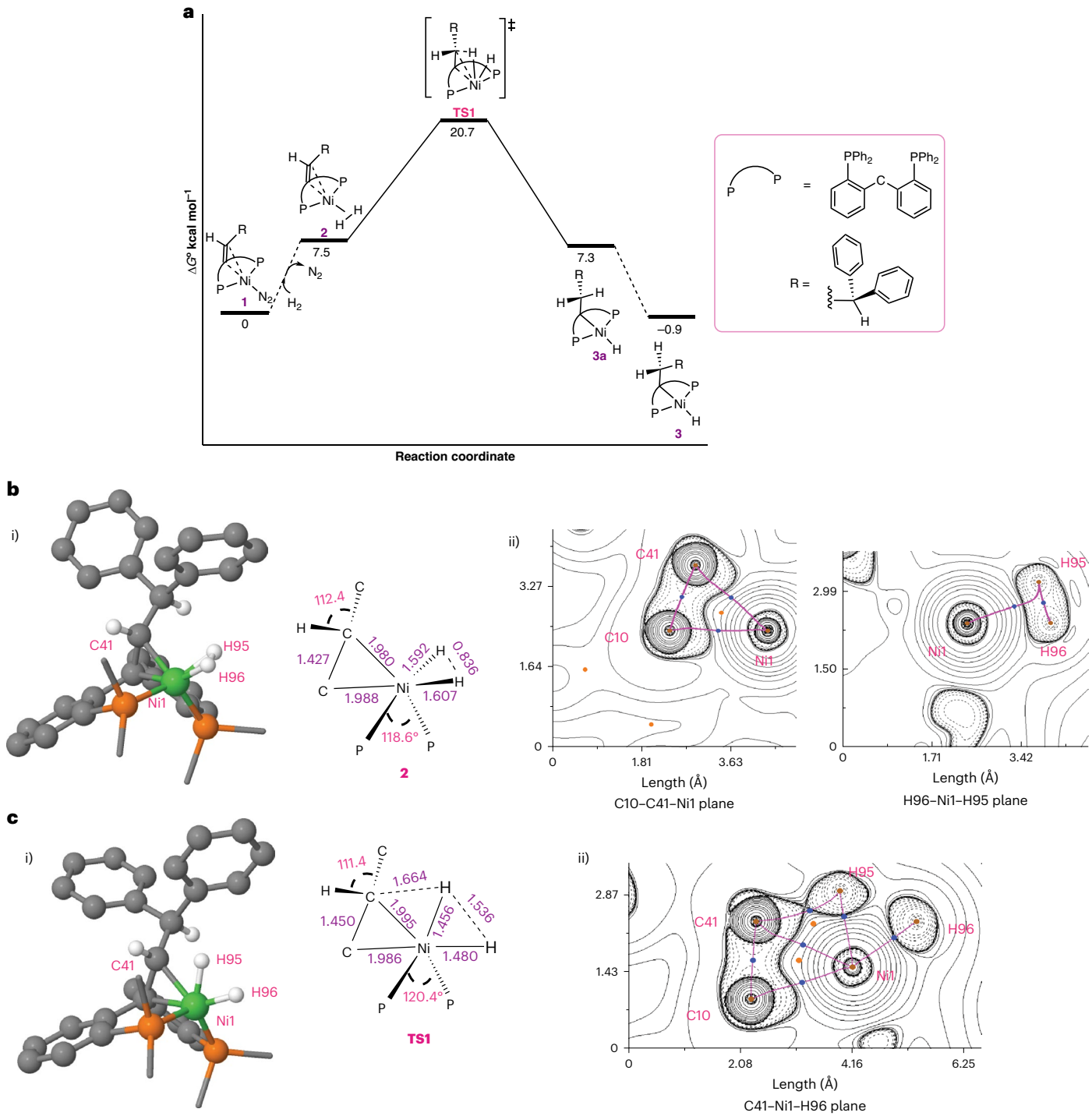

Fig. 3 | Computational studies of H_2 activation by a nickel/olefin complex. Calculations were performed at the B3LYP-GD3BJ/def2TZVP/SMD//B3LYP-GD3BJ/6-31(*d*,*p*) level of theory using toluene as the solvent. The tolyl groups were substituted by phenyl groups. Electron density for topological analysis was obtained from a single-point calculation at the B3LYP-GD3BJ/def2TZVP/SMD level of theory, with toluene as the solvent on the optimized geometry computed at B3LYP-GD3BJ/6-31(*d*,*p*) level of theory. **a**, Gibbs free energy profile for H_2 activation supporting a cooperative activation pathway. Dotted lines mark pathways for which no transition state was computed. **b**, Ni–H_2 structure analysis: (i) relevant distances (Å) and angles (°) of the optimized structure of complex **2**; (ii) two views of the Laplacian map with the positive area (ionic bond area; solid lines) and negative area (covalent bond area; dashed lines) from the QTAIM topological analysis of complex **2**. Blue dots represent BCPs, whereas orange dots are RCPs. **c**, Transition State 1 (**TS1**) structure analysis: (i) relevant distances (Å) and angles (°) of **TS1**; (ii) the Laplacian map with the positive area (ionic bond area; solid lines) and negative area (covalent bond area; dashed lines) from the QTAIM topological analysis of **TS1**.

at 1 mol%. Intriguingly, the *Z*:*E* ratio markedly changes from 12:80 to 88:9 with decreasing catalyst loading.

To understand this dependency and the reaction mechanism in general, we monitored the reaction with 10 mol% catalyst loading by ^{1}H-NMR (Fig. 4), which revealed two well-separated regimes. First, as long as diphenylacetylene is present in excess of the catalyst, clean conversion to Z-stilbene occurs with apparent zero order (Fig. 4a). Z-stilbene then starts rapidly isomerizing to *E*-stilbene to reach a

https://doi.org/10.1038/s41557-023-01380-1

Table 1 | Product ratio in the semihydrogenation of diphenylacetylene for different catalyst loadings

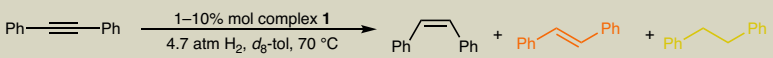

Catalyst loading (%)	Time (h)	*Z*-stilbene (%)	*E*-stilbene (%)	Diphenylethane (%)	Conversion (%)
1	43	88	9	1	98
2.5	24	51	44	5	>99
5	20	26	70	4	>99
10	22	12	80	8	>99

Reaction conditions: J Young NMR tube, pre-catalyst = complex **1**, 70 °C oil bath, volume 0.55 ml of d^8-tol, conversion and products were monitored by ^{1}H-NMR using mesitylene as internal standard.

Z:*E* ratio of ~1:2. After around 1 h, the process considerably slows down and does not reach thermodynamical equilibrium. Concomitantly, small amounts of the overhydrogenation product diphenylethane are formed.

The transition between these two regimes is accompanied by a change in catalyst speciation evidenced by operando ^{1}H-NMR and ^{31}P{^{1}H}-NMR data. In the first regime, the only observable nickel-containing species is the diphenylacetylene π-complex **4** (Fig. 4a), which also could be independently prepared by treating complex **1** with diphenylacetylene. An olefinic ^{1}H signal at δ5.72 ppm indicates that the olefin backbone decoordinates from nickel when the π-acidic alkyne binds, as has been observed for a related ketone pincer ligand (see Supplementary Section 2)[71]. Once diphenylacetylene has been consumed, complex **4** gradually disappears, which coincides with the onset of (*E*)–(*Z*) isomerization and overhydrogenation. At this time, a temporary decrease is observed in the total concentration of detected nickel species: the hydride mixture **2** ⇄ **3** probably accumulates in the reaction medium, but it cannot be detected at these concentrations because it gives broad signals (Fig. 4a, red arrow). Supporting this idea, neither (*Z*)- nor (*E*)-stilbene displaced the N_2 ligand in **1** in stoichiometric experiments, showing that these olefins cannot occupy the same binding site as diphenylacetylene in **4** (see Supplementary Section 1.4). Two new complexes gradually appear in the same period. The main species could be isolated after reaction and identified both spectroscopically and crystallographically as the *E*-stilbene complex **5** (Fig. 4b), in which the olefin backbone has been hydrogenated (self-hydrogenation). In C_6D_6 solution, **5** displays a characteristic deshielded aliphatic multiplet ^{1}H signal at δ8.38–8.52 ppm corresponding to the central C–H unit, which is indicative of an anagostic interaction with the nickel centre (H73)[72]. The Ni–C distances of 3.418(5) Å (Ni2–C73) and 3.414(5) Å (Ni1–C71) observed in the two independent molecules found in the solid-state structure of **5** are consistent with this interpretation; however, a QTAIM analysis on **5** did not identify a corresponding BCP between hydrogen and nickel, suggesting a weak interaction (see Supplementary Section 4.3). The minor species was identified as the self-hydrogenated diphenylacetylene complex **5′** (Supplementary Sections 1.3 and 1.5). When **5** and **5′** reach their final concentration, overhydrogenation stops and (*E*)–(*Z*) isomerization becomes very slow, suggesting that catalyst self-hydrogenation shuts down both pathways. Indeed, the isolated complex **5** is a sluggish isomerization catalyst under relevant conditions (10 mol%, 70 °C, 4.6 atm H_2), yielding only ~20% conversion after 24 h. Complex **5** is also inactive for the hydrogenation of diphenylacetylene (see Supplementary Section 1.5).

Isotope-labelling experiments (see Supplementary Section 1.4) rule out any participation of the allylic position in the catalytic hydrogenation mechanism. Performing the hydrogenation with D_2 expectedly results in rapid deuteration of the olefinic proton of **4**, but no deuterium incorporation at the allylic C–H position is observed (Fig. 4c). Conversely, using a deuterated analogue of complex **1** results in H/D scrambling at the olefinic position only (Fig. 4d).

The observations above suggest that the final product distribution is largely determined by the competition between (*E*)–(*Z*) isomerization and catalyst self-hydrogenation, which could be studied separately by exposing (*Z*)-stilbene to **1** (10 mol%) under an H_2 atmosphere at 70 °C (see Supplementary Section 1.3). There as well, initially rapid catalytic isomerization to (*E*)-stilbene considerably slowed down after ~2 h (~77% conversion) to reach 82% conversion after 10 h, and complex **5** was the only nickel-containing species detected by ^{1}H-NMR. In contrast, no isomerization was observed under an N_2 atmosphere, showing that complex **1** alone is inactive. These results confirm that the hydride mixture **2** ⇄ **3** generated from **1** under H_2 catalyzes olefin isomerization, presumably via a hydride mechanism, and decays to complex **5** by self-hydrogenation. Interestingly, the same reaction at 25 °C reached 93% conversion to *E*-stilbene after 10 h with barely any overhydrogenation (1%), suggesting that temperature influences the relative rates of self-hydrogenation and catalytic isomerization.

Although the self-hydrogenation process forming the inactive complex **5** could formally be initiated by C–H reductive elimination from hydride **3**, such a reaction is unlikely for *trans* substituents in a square-planar structure[41]. Accordingly, heating either **1** or its benzonitrile analogue[52] (benzonitrile is a weaker ligand than phenylacetylene) under an H_2 atmosphere does not result in any observable C–H bond formation (see Supplementary Section 1.4). By contrast, the clean formation of complex **5** from **1** and H_2 in the presence of (*E*)- or (*Z*)-stilbene suggests that an olefin acting as a hydride shuttle takes part in this process.

Density functional theory calculations performed on a slightly truncated model support the mechanistic scenario outlined in Fig. 5 (see Supplementary Section 4), which accounts for the experimental observations. The semihydrogenation cycle starts with hydride **3**. Endergonic coordination of diphenylacetylene yields complex **6** (+17.0 kcal mol^{-1}), followed by insertion ($\Delta G^{\ddagger}$ = 17.5 kcal mol^{-1}) to form the vinyl complex **7**. The transfer of a hydrogen atom from the CH_2 unit to the vinyl ligand regenerates the olefin backbone, followed by displacement of (*Z*)-stilbene for H_2 to form complex **2** (−16.9 kcal mol^{-1}). Although the overall barrier of 30.9 kcal mol^{-1} for (*Z*)-stilbene elimination is ~1 kcal mol^{-1} higher than that for H_2 cleavage, this step will be additionally favoured by concentration effects with excess alkyne[73]. Complex **2** is in an off-cycle equilibrium with resting state **4** (−33.6 kcal mol^{-1}). Rate-limiting LLHT from complex **2** with an overall activation energy of 29.9 kcal mol^{-1} regenerates hydride **3** ($\Delta G^{\ddagger}$ = −3.7 kcal mol^{-1}) and closes the cycle. Interestingly, two nearly isoenergetic pathways were identified for the C–H formation step **7** → **2**: a stepwise β-hydride elimination/reductive elimination sequence involving a high-lying nickel hydride or a concerted LLHT-like step akin to that found for H–H cleavage (see Supplementary Section 4.1)[43,44]. A σ-bond metathesis pathway cleaving the Ni–C bond of complex **7** with an incoming H_2 molecule to form **3** directly was also considered but was found energetically inaccessible with an overall barrier of 38.7 kcal mol^{-1} (see Supplementary Section 4.5). Overall, the calculated activation

https://doi.org/10.1038/s41557-023-01380-1

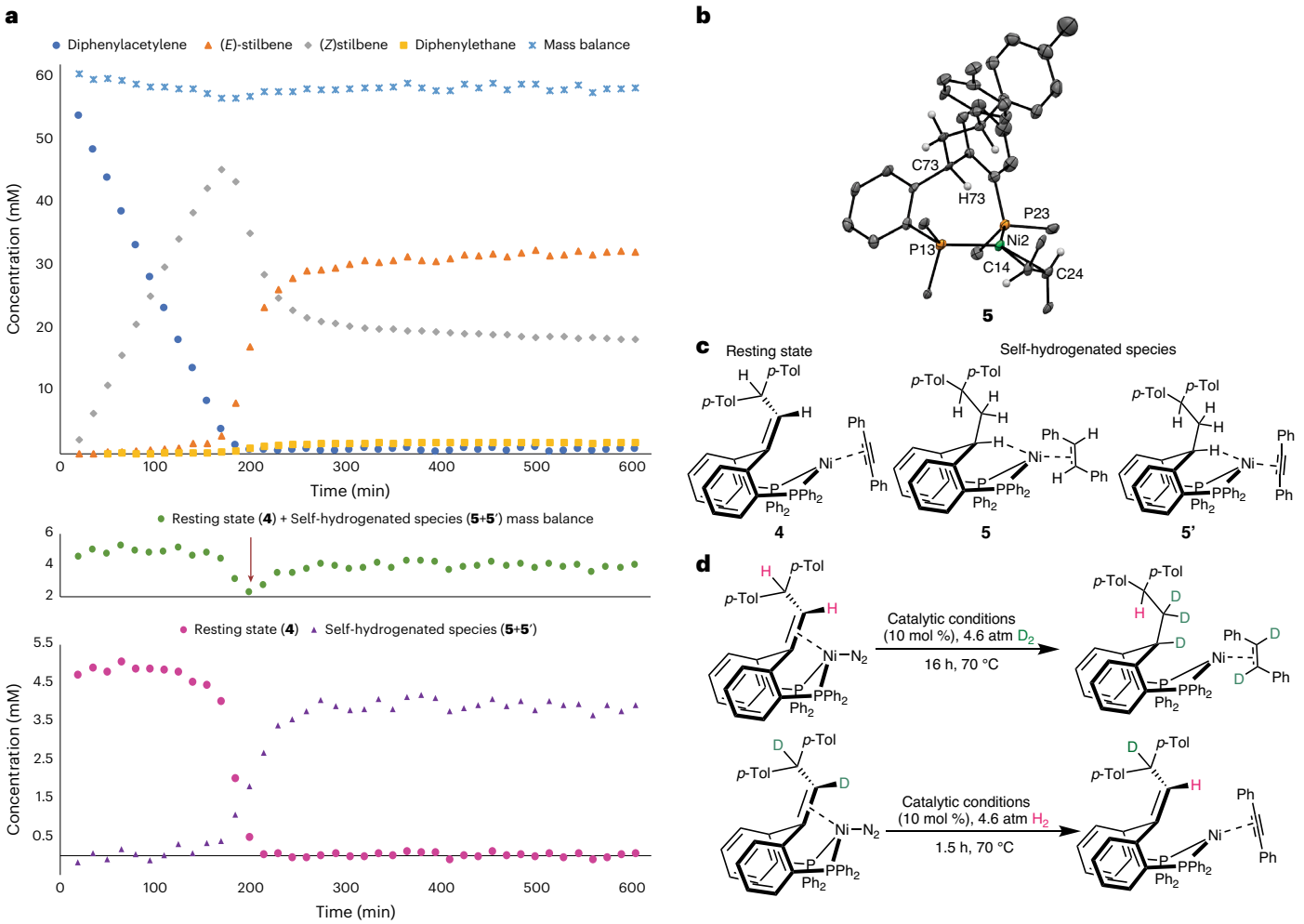

Fig. 4 | Catalytic semihydrogenation of diphenylacetylene. a, Kinetic profile recorded at 70 °C in d^8-tol with 10 mol% catalyst loading under H_2 (4.6 atm). Concentrations were determined by ^{1}H-NMR using mesitylene as the internal standard. Top: organic starting material and products. Bottom: species derived from the nickel pre-catalyst (resting state **4** and self-hydrogenated species **5** and **5′**). The green dots represent the total concentration of detected nickel-containing species and are plotted in a separate graphic for clarity. The red arrow marks a temporary decrease in the total concentration of detected species, suggesting a buildup of the hydride mixture **2** ⇄ **3** that cannot be detected under these conditions because it gives broad features. **b**, Molecular structure of self-hydrogenated product **5** determined by X-ray crystallography. Only one of two independent molecules is shown. Hexane solvent molecules and the phenyl groups of the phosphines and of the (*E*)-stilbene co-ligand are omitted for clarity. **c**, Structure of detected nickel-containing species **4, 5** and **5′**. **d**, Deuterium scrambling experiments excluding the participation of the allylic hydrogen atom ((*p*-Tol)$_2$CH) in catalysis. Top: formation of partially deuterated self-hydrogenated species **5** under catalytic conditions under D_2 atmosphere; Bottom: deuterium scrambling of d^2-complex **1** in catalytic conditions under H_2 atmosphere.

barriers for the catalytic cycle are slightly higher than those expected for a reaction taking place over hours at 70 °C (around 28.5 kcal mol^{-1}) but within the accuracy expected for DFT calculations for a relatively large system[73].

The isomerization catalytic cycle starts once diphenylacetylene has been consumed. In agreement with experiment, the associated barriers would be prohibitively high (32.5 kcal mol^{-1}) with diphenylacetylene complex **4** as a resting state, but become accessible when hydride compound **3** can accumulate in solution. Endergonic (17.9 kcal mol^{-1}) coordination of *Z*-stilbene to hydride complex **3** to form complex **8** is followed by hydride insertion ($\Delta G^{\ddagger}$ = 24.2 kcal mol^{-1}), yielding *trans*-dialkyl nickel complex **9**. Facile C–C bond rotation to form conformer **10**, followed by β-hydride elimination ($\Delta G^{\ddagger}$ = 21.9 kcal mol^{-1}), which releases *E*-stilbene to regenerate **3**, completes the isomerization cycle (see Supplementary Section 4.2).

The pathway for catalyst deactivation involves β-hydride elimination ($\Delta G^{\ddagger}$ = 24.6 kcal mol^{-1}) from structure **12** (−3.7 kcal mol^{-1}), a rotamer of **10**. The resulting complex **13** subsequently undergoes reductive elimination to form the observed complex **5**. An alternative pathway involves a concerted hydrogen transfer transition state: a hydrogen atom is transferred from one alkyl ligand to the alkyl ligand part of the pincer backbone in complex **12** with energy barrier of $\Delta G^{\ddagger}$ = 25.0 kcal mol^{-1} yielding complex **5** (see Supplementary Section 4.6). The overall barrier for self-hydrogenation is slightly higher than the isomerization process (2.7 kcal mol^{-1}), consistent with the catalyst performing a few isomerization turnovers before decaying via the thermodynamically favoured self-hydrogenation pathway. Other pathways considered were the reductive elimination from hydrides **3**, **8** or **11**, which were all prohibitively high in energy, in accordance with the difficulty of such a process for *trans* substituents in a square-planar structure. Concerted hydrogen transfer from complex **10** (no rotation) was also not feasible to yield complex **5** (see Supplementary Section 4.6).

Conclusion

In summary, we describe the cooperative activation of molecular H_2 by a nickel–olefin complex. Incorporating a precoordinated olefin

https://doi.org/10.1038/s41557-023-01380-1

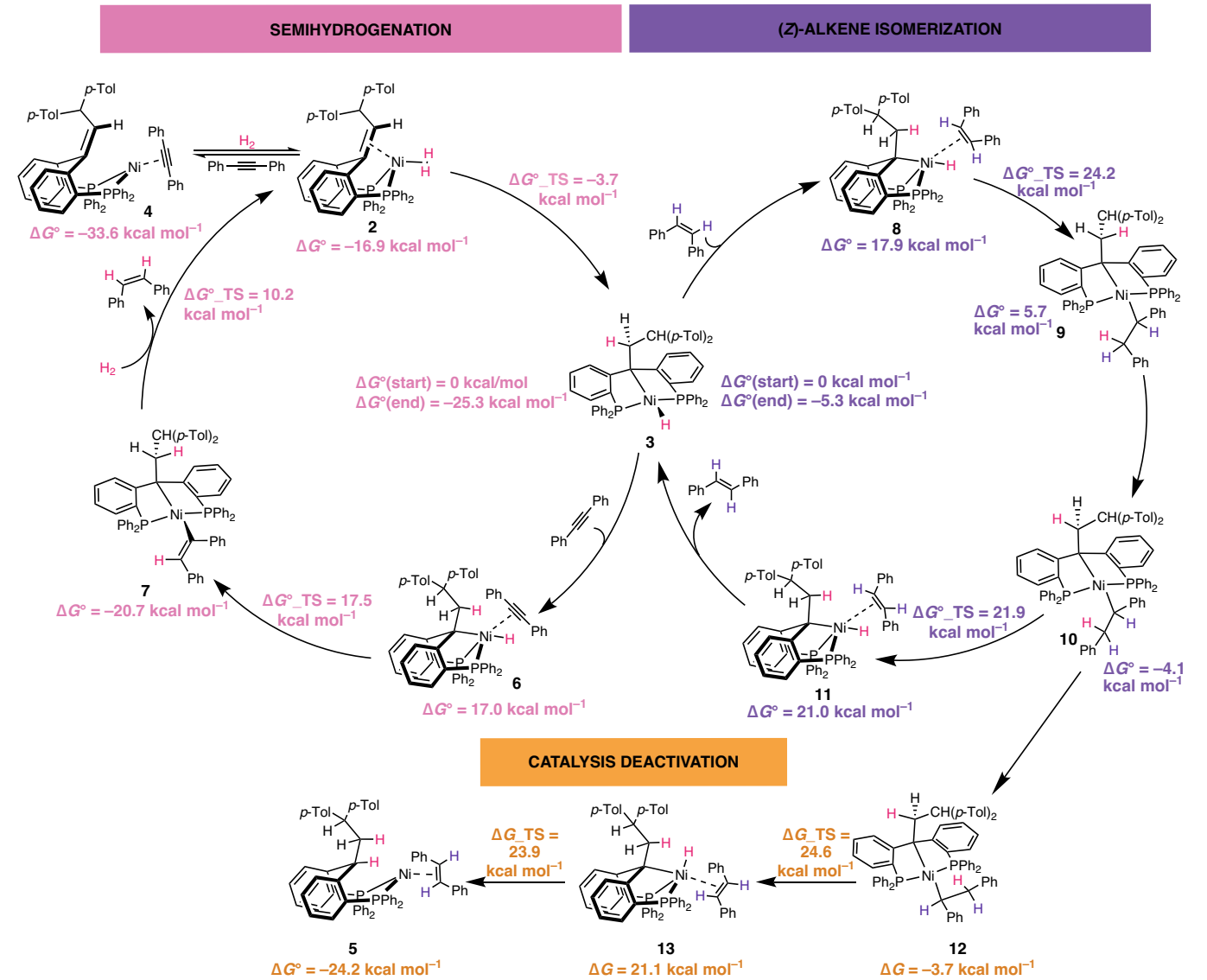

Fig. 5 | Computed catalytic cycles for semihydrogenation of diphenylacetylene and (*Z*)-stilbene isomerization, and computed pathway for the formation of complex 5. Gibbs free energies for intermediates and transition states were calculated at the B3LYP-GD3BJ/def2TZVP/SMD//B3LYP-GD3BJ/6-31(*d*,*p*) level using toluene as the solvent. In the calculations, the tolyl groups were substituted by phenyl groups, but the tolyl groups are plotted in the figure for clarity. The free energy reference Δ*G*°(start) for each catalytic cycle corresponds to the catalyst structure **3** and the starting materials. The energy associated with structure **3** at the end of the cycle (Δ*G*°(end)) corresponds to the free energy released by converting one equivalent of starting materials to products.

in a pincer ligand framework allowed for the direct observation of a rapid chemical exchange between free H_2, a non-classical (olefin) Ni–(H_2) complex, and an alkyl(hydrido) nickel(II) species by NMR spectroscopy. Experimental observations and DFT calculations support a LLHT mechanism, that is, a concerted hydrogen atom transfer from the metal-coordinated H_2 molecule to the olefin without prior oxidative addition of H_2. The reported system is an active catalyst for the semihydrogenation of diphenylacetylene using molecular H_2. Mechanistic investigations and DFT studies illustrate the importance of LLHT steps for nickel, which contrasts with heavier group 10 elements.

These results provide an experimental basis for considering LLHT steps in olefin hydrogenation mechanisms, especially with catalysts based on first-row transition metals. Furthermore, they demonstrate the potential of a tethered C=C double bond in the cooperative activation of small molecules, opening a new avenue for the design of environmentally friendly cooperative catalysts using non-noble metals.

Online content

Any methods, additional references, Nature Portfolio reporting summaries, source data, extended data, supplementary information, acknowledgements, peer review information; details of author contributions and competing interests; and statements of data and code availability are available at https://doi.org/10.1038/s41557-023-01380-1.

References

1. McGlynn, S. E. et al. Hydrogenation reactions of carbon on Earth: linking methane, margarine, and life. *Am. Mineral.* **105**, 599–608 (2020).
2. Kubas, G. J. Chemistry of saturated molecules. *Proc. Natl Acad. Sci. USA* **104**, 6901–6907 (2007).
3. Kubas, G. J. Catalytic processes involving dihydrogen complexes and other sigma-bond complexes. *Catal. Lett.* **104**, 79–101 (2005).
4. Crabtree, R. H. Dihydrogen complexation. *Chem. Rev.* **116**, 8750–8769 (2016).

5. Hale, D. J., Ferguson, M. J. & Turculet, L. (PSiP)Ni-catalyzed (*E*)-selective semihydrogenation of alkynes with molecular hydrogen. *ACS Catal*. **12**, 146–155 (2021).
6. Kubas, G. J. Activation of dihydrogen and coordination of molecular H_2 on transition metals. *J. Organomet. Chem*. **751**, 33–49 (2014).
7. Kubas, G. J. Metal–dihydrogen and σ-bond coordination: the consummate extension of the Dewar–Chatt–Duncanson model for metal–olefin π bonding. *J. Organomet. Chem*. **635**, 37–68 (2001).
8. Kubas, G. J. Fundamentals of H_2 binding and reactivity on transition metals underlying hydrogenase function and H_2 production and storage. *Chem. Rev*. **107**, 4152–4205 (2007).
9. Vollmer, M. V., Xie, J. & Lu, C. C. Stable dihydrogen complexes of cobalt(–I) suggest an inverse *trans*-influence of Lewis acidic group 13 metalloligands. *J. Am. Chem. Soc*. **139**, 6570–6573 (2017).
10. Jessop, P. G. & Morris, R. H. Reactions of transition metal dihydrogen complexes. *Coord. Chem. Rev*. **121**, 155–284 (1992).
11. Alig, L., Fritz, M. & Schneider, S. First-row transition metal (de) hydrogenation catalysis based on functional pincer ligands. *Chem. Rev*. **119**, 2681–2751 (2019).
12. Manar, K. K. & Ren, P. in *Advances in Organometallic Chemistry* Vol. 76 (Elsevier Inc., 2021).
13. Karunananda, M. K. & Mankad, N. P. Cooperative strategies for catalytic hydrogenation of unsaturated hydrocarbons. *ACS Catal*. **7**, 6110–6119 (2017).
14. Grotjahn, D. B. Bifunctional organometallic catalysts involving proton transfer or hydrogen bonding. *Chem. Eur. J*. **11**, 7146–7153 (2005).
15. Tiddens, M. R. & Moret, M.-E. *Top. Organomet. Chem*. **68**, 25–69 (2021).
16. Elsby, M. R. & Baker, R. T. Strategies and mechanisms of metal–ligand cooperativity in first-row transition metal complex catalysts. *Chem. Soc. Rev*. **49**, 8933–8987 (2020).
17. Milstein, D. Metal–ligand cooperation by aromatization–dearomatization as a tool in single bond activation. *Philos. Trans. R. Soc. A* **373**, 20140189 (2015).
18. Van Der Vlugt, J. I. Cooperative catalysis with first-row late transition metals. *Eur. J. Inorg. Chem*. **2012**, 363–375 (2012).
19. Grützmacher, H. Cooperating ligands in catalysis. *Angew. Chem. Int. Ed*. **47**, 1814–1818 (2008).
20. He, T. et al. Mechanism of heterolysis of H_2 by an unsaturated d^8 nickel center: via tetravalent nickel. *J. Am. Chem. Soc*. **132**, 910–911 (2010).
21. Schneider, S., Meiners, J. & Askevold, B. Cooperative aliphatic PNP amido pincer ligands-versatile building blocks for coordination chemistry and catalysis. *Eur. J. Inorg. Chem*. **2012**, 412–429 (2012).
22. Harman, W. H. & Peters, J. C. Reversible H_2 addition across a nickel-borane unit as a promising strategy for catalysis. *J. Am. Chem. Soc*. **134**, 5080–5082 (2012).
23. Harman, W. H., Lin, T. P. & Peters, J. C. A d^{10} Ni–(H_2) adduct as an intermediate in H–H oxidative addition across a Ni–B bond. *Angew. Chem. Int. Ed*. **53**, 1081–1086 (2014).
24. Karunananda, M. K. & Mankad, N. P. *E*-selective semi-hydrogenation of alkynes by heterobimetallic catalysis. *J. Am. Chem. Soc*. **137**, 14598–14601 (2015).
25. Kubas, G. J., Ryan, R. R., Swanson, B. I., Vergamini, P. J. & Wasserman, H. J. Characterization of the first examples of isolable molecular hydrogen complexes, $M(CO)_3(PR_3)_2(H_2)$. *J. Am. Chem. Soc*. **106**, 451–452 (1984).
26. Bianchini, C. et al. Selective hydrogenation of 1-alkynes to alkenes catalyzed by an iron(II) *cis*-hydride η^2-dihydrogen complex. A case of intramolecular reaction between η^2-H_2 and-σ-vinyl ligands. *Organometallics* **11**, 138–145 (1992).
27. Thomas, A., Haake, M., Grevels, F. -W. & Bargon, J. In situ NMR investigations of photocatalyzed hydrogenations with parahydrogen in the presence of metal carbonyl compounds of group 6. *Angew. Chem. Int. Ed*. **33**, 755–757 (1994).
28. Joshi, A. M., MacFarlane, K. S. & James, B. R. Kinetics and mechanism of H_2-hydrogenation of styrene catalyzed by $[RuCl(dppb)\ (\mu\text{-}Cl)]_2$ (dppb=1,4-bis(dipphenylphosphino)butane). Evidence for hydrogen transfer from a dinuclear molecular hydrogen species. *J. Organomet. Chem*. **488**, 161–167 (1995). .
29. Kirss, R. U., Eisenschmid, T. C. & Eisenberg, R. *Para*-hydrogen induced polarization in hydrogenation reactions catalyzed by ruthenium-phosphine complexes. *J. Am. Chem. Soc*. **110**, 8564–8566 (1988).
30. Jia, G., Ng, W. S. & Lau, C. P. Dihydrogen complex formation and C–C bond cleavage from protonation of Cp*RuH(diene) complexes. *Organometallics* **17**, 4538–4540 (1998).
31. Kubas, G. J. *Metal Dihydrogen and σ-Bond Complexes* (Springer, 2001); https://doi.org/10.1007/b113929
32. Vigalok, A., Kraatz, H., Konstantinovsky, L. & Milstein, D. Evidence for direct *trans* insertion in a hydrido–olefin rhodium complex—free nitrogen as a trap in a migratory insertion process. *Chem. Eur. J* **3**, 253–260 (1997).
33. Polukeev, A. V. & Wendt, O. F. Iridium pincer complexes with an olefin backbone. *Organometallics* **34**, 4262–4271 (2015).
34. Polukeev, A. V. & Wendt, O. F. Iridium complexes with aliphatic, non-innocent pincer ligands. *J. Organomet. Chem*. **867**, 33–50 (2018).
35. Verhoeven, D. G. A. & Moret, M. E. Metal-ligand cooperation at tethered π-ligands. *Dalton Trans*. **45**, 15762–15778 (2016).
36. Comanescu, C. C., Vyushkova, M. & Iluc, V. M. Palladium carbene complexes as persistent radicals. *Chem. Sci*. **6**, 4570–4579 (2015).
37. Barrett, B. J. & Iluc, V. M. An adaptable chelating diphosphine ligand for the stabilization of palladium and platinum carbenes. *Organometallics* **36**, 730–741 (2017).
38. Barrett, B. J. & Iluc, V. M. Group 10 metal complexes supported by pincer ligands with an olefinic backbone. *Organometallics* **33**, 2565–2574 (2014).
39. Barrett, B. J. & Iluc, V. M. Coordination of a hemilabile pincer ligand with an olefinic backbone to mid-to-late transition metals. *Inorg. Chem*. **53**, 7248–7259 (2014).
40. Breitenfeld, J., Vechorkin, O., Corminboeuf, C., Scopelliti, R. & Hu, X. Why are (NN_2)Ni pincer complexes active for alkyl–alkyl coupling: β-H elimination is kinetically accessible but thermodynamically uphill. *Organometallics* **29**, 3686–3689 (2010).
41. Crabtree, R. H. *The Organometallic Chemistry of the Transition Metals* (John Wiley & Sons, 2014); https://doi.org/10.1002/9781118788301
42. Michaliszyn, K., Smirnova, E. S., Bucci, A., Martin-Diaconescu, V. & Lloret Fillol, J. Well-defined nickel P_3C complexes as hydrogenation catalysts of *N*-heteroarenes under mild conditions. *ChemCatChem* **14**, e202200039 (2022).
43. Guihaumé, J., Halbert, S., Eisenstein, O. & Perutz, R. N. Hydrofluoroarylation of alkynes with Ni catalysts. C–H activation via ligand-to-ligand hydrogen transfer, an alternative to oxidative addition. *Organometallics* **31**, 1300–1314 (2012).
44. Perutz, R. N., Sabo-Etienne, S. & Weller, A. S. Metathesis by partner interchange in σ-bond ligands: expanding applications of the σ-CAM mechanism. *Angew. Chem. Int. Ed*. **61**, e202111462 (2022).
45. Tang, S., Eisenstein, O., Nakao, Y. & Sakaki, S. Aromatic C–H σ-bond activation by Ni^0, Pd^0 and Pt^0 alkene complexes: concerted oxidative addition to metal vs ligand-to-ligand H transfer mechanism. *Organometallics* **36**, 2761–2771 (2017).
46. Perutz, R. N. & Sabo-Etienne, S. The σ-CAM mechanism: σ complexes as the basis of σ-bond metathesis at late-transition-metal centers. *Angew. Chem. Int. Ed*. **46**, 2578–2592 (2007).

47. Murugesan, K. et al. Nickel-catalyzed stereodivergent synthesis of *E*- and *Z*-alkenes by hydrogenation of alkynes. *ChemSusChem* **12**, 3363–3369 (2019).
48. Ramirez, B. L. & Lu, C. C. Rare-earth supported nickel catalysts for alkyne semihydrogenation: chemo- and regioselectivity impacted by the Lewis acidity and size of the support. *J. Am. Chem. Soc.* **142**, 5396–5407 (2020).
49. Thiel, N. O., Kaewmee, B., Tran Ngoc, T. & Teichert, J. F. A simple nickel catalyst enabling an *E*-selective alkyne semihydrogenation. *Chem. Eur. J.* **26**, 1597–1603 (2020).
50. Swamy, K. C. K., Reddy, A. S., Sandeep, K. & Kalyani, A. Advances in chemoselective and/or stereoselective semihydrogenation of alkynes. *Tetrahedron Lett.* **59**, 419–429 (2018).
51. Gregori, B. J., Schmotz, M.-O. W. S. & Jacobi von Wangelin, A. Stereoselective semi-hydrogenations of alkynes by first-row (3d) transition metal catalysts. *ChemCatChem* **14**, e202200886 (2022).
52. Sansores-Paredes, M. L. G., Voort, S., Lutz, M. & Moret, M. Divergent reactivity of an isolable nickelacyclobutane. *Angew. Chem. Int. Ed.* **60**, 26518–26522 (2021).
53. Gullett, K. L. et al. *Dihydrogen and Dinitrogen Complexes of Cobalt and Nickel. Comprehensive Coordination Chemistry III* Vol. 6 (Elsevier, 2021).
54. Morris, R. H. Dihydrogen, dihydride and in between: NMR and structural properties of iron group complexes. *Coord. Chem. Rev.* **252**, 2381–2394 (2008).
55. Luther, T. A. & Heinekey, D. M. Synthesis, characterization, and reactivity of dicationic dihydrogen complexes of osmium and ruthenium. *Inorg. Chem.* **37**, 127–132 (1998).
56. Cammarota, R. C. & Lu, C. C. Tuning nickel with Lewis acidic group 13 metalloligands for catalytic olefin hydrogenation. *J. Am. Chem. Soc.* **137**, 12486–12489 (2015).
57. Cammarota, R. C. et al. Thermodynamic and kinetic studies of H_2 and N_2 binding to bimetallic nickel-group 13 complexes and neutron structure of a Ni(η^2-H_2) adduct. *Chem. Sci.* **10**, 7029–7042 (2019).
58. Connor, B. A., Rittle, J., Vandervelde, D. & Peters, J. C. A Ni^0(η^2-(Si–H))(η^2-H_2) complex that mediates facile H atom exchange between two σ-ligands. *Organometallics* **35**, 686–690 (2016).
59. Tsay, C. & Peters, J. C. Thermally stable N_2 and H_2 adducts of cationic nickel(II). *Chem. Sci.* **3**, 1313–1318 (2012).
60. Connelly, S. J., Zimmerman, A. C., Kaminsky, W. & Heinekey, D. M. Synthesis, structure, and reactivity of a nickel dihydrogen complex. *Chem. Eur. J.* **18**, 15932–15934 (2012).
61. Robinson, S. J. C. & Heinekey, D. M. Hydride & dihydrogen complexes of earth abundant metals: structure, reactivity, and applications to catalysis. *Chem. Commun.* **53**, 669–676 (2017).
62. Prat, J. R., Cammarota, R. C., Graziano, B. J., Moore, J. T. & Lu, C. C. Toggling the Z-type interaction off-on in nickel-boron dihydrogen and anionic hydride complexes. *Chem. Commun.* **58**, 8798–8801 (2022).
63. Cammarota, R. C. et al. A bimetallic nickel–gallium complex catalyzes CO_2 hydrogenation via the intermediacy of an anionic d^{10} nickel hydride. *J. Am. Chem. Soc.* **139**, 14244–14250 (2017).
64. Lu, T. & Chen, F. Multiwfn: a multifunctional wavefunction analyzer. *J. Comput. Chem.* **33**, 580–592 (2012).
65. Vastine, B. A. & Hall, M. B. Carbon–hydrogen bond activation: two, three, or more mechanisms? *J. Am. Chem. Soc.* **129**, 12068–12069 (2007).
66. Skipper, C. V. J., Hoang, T. K. A., Antonelli, D. M. & Kaltsoyannis, N. Transition metal hydrazide-based hydrogen-storage materials: the first atoms-in-molecules analysis of the Kubas interaction. *Chem. Eur. J.* **18**, 1750–1760 (2012).
67. Sparkes, H. A., Chaplin, A. B., Weller, A. S. & Howard, J. A. K. Bond catastrophes in rhodium complexes: experimental charge-density studies of [Rh(C_7H_8)(P^tBu_3)Cl] and [Rh(C_7H_8)(PCy_3)Cl]. *Acta Crystallogr. B* **66**, 503–514 (2010).
68. Bair, J. S. et al. Linear-selective hydroarylation of unactivated terminal and internal olefins with trifluoromethyl-substituted arenes. *J. Am. Chem. Soc.* **136**, 13098–13101 (2014).
69. Chen, M. & Montgomery, J. Nickel-catalyzed intermolecular enantioselective heteroaromatic C–H alkylation. *ACS Catal.* **12**, 11015–11023 (2022).
70. Saper, N. I. et al. Nickel-catalysed anti-Markovnikov hydroarylation of unactivated alkenes with unactivated arenes facilitated by non-covalent interactions. *Nat. Chem.* **12**, 276–283 (2020).
71. Orsino, A. F., Gutiérrez Del Campo, M., Lutz, M. & Moret, M. E. Enhanced catalytic activity of nickel complexes of an adaptive diphosphine-benzophenone ligand in alkyne cyclotrimerization. *ACS Catal.* **9**, 2458–2481 (2019).
72. Lesueur, W., Solari, E., Floriani, C., Chiesi-Villa, A. & Rizzoli, C. A bidentate bisphosphine functioning in intramolecular aliphatic metalation and as an NMR spectroscopic probe for the metal coordination environment. *Inorg. Chem.* **36**, 3354–3362 (1997).
73. Ryu, H. et al. Pitfalls in computational modeling of chemical reactions and how to avoid them. *Organometallics* **37**, 3228–3239 (2018).

Methods

General information

All reactants were purchased from commercial sources and used as received without further purification unless otherwise noted; (*E*)-stilbene, (*Z*)-stilbene and diphenylacetylene were stored in the glovebox. Furthermore, (*Z*)-stilbene and mesitylene were degassed by three freeze–pump–thaw cycles before use.

All of the reactions were performed under an N_2(g) atmosphere in the glovebox. Deuterated solvents were purchased from Cambridge Isotope Laboratory Inc., degassed by three freeze–pump–thaw cycles, and stored over molecular sieves before use. Common solvents were dried using a MBRAUN MB SPS-80 purification system and/or distillation technique; [(^{Ph}bppe$^{H,CH^pTol_2}$)Ni]N_2 and [(^{Ph}bppe$^{H,CH^pTol_2}$)Ni]PhCN were synthetized according to literature procedures[52].

Physical methods

^{1}H, ^{13}C and ^{31}P-NMR spectra (400, 100 and 161 MHz respectively) were recorded on an Agilent MR400 or a Varian AS400 spectrometer at 297 K unless stated otherwise. ^{1}H and ^{13}C-NMR chemical shifts relative to tetramethylsilane are referenced to the residual solvent resonance unless stated otherwise. ^{31}P-NMR chemical shifts were externally referenced to 85% aqueous H_3PO_4. Infrared spectra were recorded using a Perkin-Elmer Spectrum One Fourier-transform infrared spectrometer under N_2 flow. Gas chromatography analyses were performed on a Perkin-Elmer Clarus 500 GC (column PE, Elite-5, 30 m × 0.32 mm × 0.25 µm, (5% phenyl):(95% methyl)polysiloxane)) and a flame-ionization detector.

General catalysis procedure

Stock solutions of catalyst (0.012 M) and diphenylacetylene (0.1 M) in deuterated toluene were prepared in the glovebox. In a vial, 0.25 ml of catalyst solution and 0.3 ml of diphenylacetylene solution were added, turning the solution red; 4.2 µl of mesitylene was added to the solution with a microsyringe and then mixed. The reaction mixture was transferred to a J Young NMR tube. The tube was connected to a gas set-up and degassed by two freeze–pump–thaw cycles, and hydrogen gas was introduced to the solution inside of a Dewar with liquid nitrogen. The solution was warmed up to room temperature and analysed, and then placed in an oil bath at 70 °C. The concentrations of the products were determined by ^{1}H-NMR using mesitylene as internal standard. Proton peaks used in quantification (d^8-tol, 400 MHz)[48]: diphenylacetylene, 7.46 (m, 4H); (*E*)-stilbene, 7.29 (dd, *J* = 8.3, 1.3 Hz, 4H); (*Z*)-stilbene, 6.44 (s, 2H); 1,2-diphenylethane, 2.72 (s, 1H); mesitylene, 6.67 (s, 3H).

Mercury drop experiment procedure

Two Schlenk bombs with stirring bars (one containing a drop of mercury) were charged with 0.25 ml of a stock solution (0.012 M) of catalyst and 0.6 ml of a stock solution of diphenylacetylene (0.1 M) in toluene (total volume = 0.85 ml); 4.2 µl of mesitylene was added to the solution with a microsyringe and mixed. Both Schlenks were connected to a gas set-up, degassed twice by a freeze–pump procedure and hydrogen gas was introduced. Both Schlenk bombs were heated under intense stirring for 5 h at 70 °C. After this time, the pressure was released; 0.0062 mmol of dodecane, 5 ml of Et_2O and 1 ml of water were added. The organic phase was extracted, and 1 ml of acetone was added to dilute the mixture. The solution was analysed by gas chromatograph–flame-ionization detector and no difference was found in the product concentration.

Experimental procedure for kinetic profiles

Stock solutions of catalyst (0.012 M), (*Z*)-stilbene and diphenylacetylene (0.1 M) in deuterated toluene were prepared in the glovebox. In a vial, 0.25 ml of catalyst solution and 0.3 ml of each substrate solution were added as needed (semihydrogenation and isomerization profiles volume = 0.55 ml; competition catalyst = 0.85 ml); 4.2 µl of mesitylene was added to the solution with a microsyringe and mixed. The reaction mixture was transferred to a J Young NMR tube. The tube was connected to a gas set-up and degassed by two freeze–pump–thaw cycles, and hydrogen gas was introduced to the solution inside of a Dewar with liquid nitrogen. The solution was warmed up to room temperature and introduced into the NMR spectrometer at either 25 or 70 °C.

Data analysis for kinetic profiles

Kinetic profiles were monitored by ^{1}H-NMR spectroscopy using mesitylene as internal standard. Proton peaks used in quantification (d^8-tol, ppm, 400 MHz)[48]: diphenylacetylene, 7.46 (m, 4H); (*E*)-stilbene, 7.29 (dd, *J* = 8.3, 1.3 Hz, 4H); (*Z*)-stilbene, 6.44 (s, 2H); 1,2-diphenylethane, 2.72 (s, 1H); mesitylene, 6.67 (s, 3H), 2.13 (s, 9H). Resting state, complex **4**, 2.23 (s, 3H); self-hydrogenated catalyst, complex **5**, 5.83 (d, 2H) or 2.20 (s, 3H); self-hydrogenated catalyst, complex **5′**, 2.23 (s, 3H).

The aromatic peak of the internal standard (6.67 ppm) was used for quantification in all profiles except for the isomerization at 25 °C, where the aliphatic peak was used (2.13 ppm). The data were processed using the MestReNova program, with the data analysis on arrayed spectra. The information was extracted by peak area integration for all kinetic profiles except the catalysis analysis[74]. For the kinetic profiles that involved semihydrogenation, a background correction was applied on (*E*)-stilbene by withdrawing the first value of the integration to all of the points (to subtract some intensity corresponding to the resting state). In case of the catalysis analysis in the semihydrogenation profile this was extracted based on the peak height, which is recommended if peaks of interest have some degree of overlapping[74]. A background correction was applied to the resting state and self-hydrogenated products to decrease the effects of noise on the spectra. The average of the value of the last six points for the resting state was subtracted from all points. In case of the self-hydrogenated products, the average of the value of the first six points was subtracted.

X-ray crystal structure determination of self-hydrogenated catalyst (5)

$C_{67}H_{58}NiP_2{\cdot}C_6H_{14}$, Formula weight (Fw) = 1,069.95, red needle, 0.39 × 0.06 × 0.06 mm^3, monoclinic, $P2_1/n$ (no. 14), a = 10.2716(6), b = 24.0789(12), c = 46.997(3) Å, β = 92.130(3)°, unit cell volume (V) = 11615.7(12) Å^3, number of formula units in the unit cell (Z) = 8, density of the crystal determined from the X-ray crystal structure (D_x) = 1.224 g cm^{-3} and absorption coefficient of the crystal (μ) = 0.43 mm^{-1}. The diffraction experiment was performed on a Bruker Kappa ApexII diffractometer with a sealed tube and Triumph monochromator (λ = 0.71073 Å) at a temperature of 150(2) K up to a resolution of $(\sin\theta/\lambda)_{max}$ = 0.57 Å^{-1}. The Eval15 software[75] was used for the intensity integration. The crystal structure was characterized by pseudo-translational symmetry (pseudo-I-centred Bravais lattice). Consequently many reflections are weak or very weak. A numerical absorption correction and scaling was performed with SADABS[76] (correction range 0.84–0.98). A total of 114,418 reflections was measured, 18,328 reflections were unique (R_{int} = 0.223), 8,209 reflections were observed [$I > 2\sigma(I)$]. The structure was solved with Patterson superposition methods using SHELXT[77]. Structure refinement was performed with SHELXL-2018[78] on F^2 of all reflections. Non-hydrogen atoms were refined freely with anisotropic displacement parameters. The *n*-hexane solvent molecules were refined with a disorder model. The hydrogen atoms of the metal complexes were located in difference Fourier maps, the hydrogen atoms of the solvent were introduced in calculated positions. Hydrogens H71 and H73 were kept fixed at their located positions. All other hydrogen atoms were refined using a riding model; 1,483 parameters were refined with 2,242 restraints (displacement parameters of all atoms, distances and angles in the disordered *n*-hexane molecules). R1/wR2 [$I > 2\sigma(I)$], 0.0682/0.1363; R1/wR2 (all refl.), 0.1865/0.1793; S = 0.996; residual electron density between

−0.51 and 0.79 e Å^{-3}. Geometry calculations and checking for higher symmetry was performed using the PLATON program[79,80].

Computational methods

Density functional theory calculations were performed using the Gaussian 16 software package v.C.01 (ref. 80). The tolyl groups in the structure were substituted by phenyl groups for simplicity. Geometry optimizations were performed in vacuum at the B3LYP-GDB3J/6-31 g(*d*,*p*) level of theory on all atoms. Frequency analyses on all stationary points were used to ensure that they are minima (no imaginary frequency) or transition states (one imaginary frequency). Transition states were calculated using the synchronous transit-guided quasi-Newton number 3 (QST3) method or using the opt = TS (Berny algorithm) keyword. The guess structure proposed for each transition state calculation was based on the results of relaxed potential energy surface scans; Δ*G*° was calculated by single-point calculation at B3LYP-GDB3J/def2TZVP/SMD(toluene) level of theory adjusting the value with the thermal correction obtained at the B3LYP-GDB3J/6-31 g(*d*,*p*) level of theory at 298.15 K and 1 atm. Furthermore, geometry optimization energies and single-point energies were compared (see Supplementary Section 4.8) to verify that no major discrepancy indicative of an insufficient basis set for geometry optimization was observed. QTAIM analysis was perfomed on the single-point calculation at B3LYP-GDB3J/def2TZVP/SMD(toluene) level of theory using the Multiwfn program[64].

Equilibrium under hydrogen gas (^{Ph}bppe$^{H,CH^{p}Tol_2}$)Ni(H$_2$) (2) and [PCH$_2$CH(*p*-Tol)$_2$P]NiH (3)

[(^{Ph}bppe$^{H,CH^{p}Tol_2}$)Ni]$_2$ (μ-N$_2$) (**1^{dimer}**, 10 mg, 0.006 mmol) was dissolved in 0.5 ml of *d*^{8}-toluene and the solution was placed in a J Young NMR tube. The sample was degassed by two freeze–pump–thaw cycles and hydrogen gas was introduced while the tube was immersed in liquid nitrogen. The solution was warmed up to room temperature and analysed. If the sample is degassed again by two freeze–pump–thaw cycles and nitrogen gas is reintroduced, complex (^{Ph}bppe$^{H,CH^{p}Tol_2}$)Ni(N$_2$) is regenerated.

Equilibrium mixture at 25 °C: ^{1}H-NMR (400 MHz, *d*^{8}-tol, 25 °C): *δ* (ppm) *δ*7.64 (b, 6H), 7.26 (m, 3H), 7.17 (b, 8H), 6.94–6.84 (m, 10H), 6.79 (b, 9H), 3.84 (s, 1H, C*H*), 2.09 (s, 6H), −14.41 (s, 1H, Ni–*H*). Some peaks are overlapping with the residual solvent signals.

^{31}P{H^1}-NMR (162 MHz, *d*^{8}-tol, 25 °C): *δ* (ppm) 40.1 (s, 2P).

Equilibrium mixture at −40 °C: ^{1}H-NMR (400 MHz, *d*^{8}-tol, −40 °C): *δ* (ppm) *δ*7.84–7.74 (m, 2H), 7.68 (d, *J* = 8.1 Hz, 2H), 7.54 (s, 4H), 7.45 (d, *J* = 7.7 Hz, 1H), 7.38–7.18 (m, 11H), 6.95–6.85 (m, 12H), 6.84–6.73 (m, 11H), 4.76 (s, CH_{olefin} complex 1), 4.40 (s, CH_{olefin} complex 2), 3.80 (t, $^3J_{H,H}$ = 8.4 Hz, 1H, C*H*), 3.12 (b, 2H, CH_2), −2.09 (b, Ni–H_2), −14.29 (t, $^2J_{H,P}$ = 64.3 Hz, 1H, Ni–*H*).

^{13}C{H^1}-NMR (101 MHz, *d*^{8}-tol, −40 °C): *δ* (ppm) 164.0 (s, Ar), 150.3 (s, Ar), 143.9 (s, Ar), 141.9–140.8 (m, Ar), 139.1 (s, Ar), 138.5–137.6 (m, Ar), 135.1–134.3 (m, Ar), 133.8 (s, Ar), 133.6 (s, Ar), 133.3 (s, Ar), 129.8 (d, *J* = 10.6 Hz), 129.3–129.0 (m, Ar), 125.7 (s, Ar), 125.5 (s, Ar), 65.0 (s, *C*-CH$_2$), 56.9 (s, *C*H$_2$), 50.8 (s, *C*H), 21.3 (s, *C*H$_3$), 21.0 (s, *C*H$_3$).

^{31}P{H^1}-NMR (162 MHz, *d*^{8}-tol, −40 °C): *δ* (ppm) 40.6 (s, 2P), 28.2 (d, $^2J_{P,P}$ = 53.3 Hz, 1P), 32.8 (d, $^2J_{P,P}$ = 60.2 Hz, 1P), 15.5 (d, $^2J_{P,P}$ = 58.7 Hz, 1P), 11.3 (d, $^2J_{P,P}$ = 53.6 Hz, 1P).

Characteristic peaks (**2**): ^{1}H-NMR (400 MHz, *d*^{8}-tol, −40 °C): *δ* (ppm) 4.40 (s, 1H, CH_{olefin}), −2.09 (b, 2H, H_2); ^{31}P{H^1}-NMR (162 MHz, *d*^{8}-tol, −40 °C): *δ* (ppm) 32.8 (d, $J_{P,P}$ = 60.2 Hz, 1P), 15.5 (d, $J_{P,P}$ = 58.7 Hz, 1P).

Characteristic peaks (**3**): ^{1}H-NMR (400 MHz, *d*^{8}-tol, −40 °C): *δ* (ppm) 3.80 (t, 1H, C*H*), 3.12 (b, 2H, CH_2), −14.29 (t, $J_{H,P}$ = 64.3 Hz, 1H, Ni–*H*); ^{31}P{H^1}-NMR (162 MHz, *d*^{8}-tol, −40 °C): *δ* (ppm) 40.6 (s, 2P); ^{13}C{H^1}-NMR (101 MHz, *d*^{8}-tol, −40 °C): *δ* (ppm) 56.9 (s, *C*H$_2$), 50.8 (s, *C*H).

Synthesis of [(^{Ph}bppe$^{H,CH^{p}Tol_2}$)Ni(PhCCPh) (4)

[(^{Ph}bppe$^{H,CH^{p}Tol_2}$)Ni]$_2$(μ-N$_2$) (**1^{dimer}**, 50 mg, 0.030 mmol) was weighed in a vial and dissolved in toluene (5 ml). Diphenylacetylene (11 mg, 0.062 mmol) dissolved in toluene (1 ml) was added at once and the solution was stirred for 5 h. Afterwards, the solution was concentrated to approximately 1 ml under vacuum. Hexane (1 ml) was added to the solution, which was cooled down to −35 °C for 15 min. The precipitate was separated by decantation, washed with cold hexane twice and dried to obtain the product as a yellow powder (53 mg, 90 % yield). The high sensitivity of the compound did not allow to obtain elemental analysis and HRMS data.

^{1}H-NMR (400 MHz, C$_6$D$_6$, 25 °C): *δ* (ppm) 7.52 (dt, *J* = 6.9, 1.3 Hz, 2H, Ar–*H*), 7.46–7.40 (m, 2H, Ar–*H*), 7.32–7.25 (m, 3H, Ar–*H*), 7.10 (d, *J* = 7.8 Hz, 2H, Ar–*H*), 7.03–6.91 (m, 14H, Ar–*H*), 6.91–6.82 (m, 10H, Ar–*H*), 6.81–6.75 (m, 5H, Ar–*H*), 6.74 (t, *J* = 1.5 Hz, 1H, Ar–*H*), 6.69 (td, *J* = 7.5, 1.2 Hz, 1H, Ar–*H*), 5.72 (d, *J* = 10.5 Hz, 1H, =C*H*R), 4.68 (d, *J* = 10.5 Hz, 1H, C*Hp*-Tol$_2$), 2.26 (s, 3H, CH_3), 2.06 (s, 3H, CH_3).

^{13}C{H^1}-NMR (101 MHz, C$_6$D$_6$, 25 °C): *δ* (ppm) 150.9 (d, *J* = 27.5 Hz, Ar), 143.2 (d, *J* = 3.4 Hz, Ar), 141.3 (s, Ar), 139.7 (d, *J* = 26.7 Hz, Ar), 138.7 (d, *J* = 21.7 Hz, Ar), 137.4 (s, Ar), 137.2 (s, Ar), 137.1 (s, Ar), 136.9 (d, *J* = 10.3 Hz, Ar), 136.5 (s, Ar), 136.3 (s, Ar), 136.0 (s, Ar), 135.3 (s, Ar), 135.3 (s, Ar), 135.1 (s, Ar), 134.9 (s, Ar), 133.9 (d, *J* = 13.2 Hz, Ar), 133.6 (d, *J* = 13.3 Hz, Ar), 133.4–133.1 (m, Ar), 131.9 (s, Ar), 131.2 (d, *J* = 9.2 Hz, Ar), 130.6 (d, *J* = 10.0 Hz, Ar), 129.4 (d, *J* = 15.3 Hz, Ar), 129.1 (s, Ar), 129.0 (s, Ar), 128.8–128.5 (m, Ar), 124.5 (s, Ar or =*C*H) 52.2 (s, *C*H*p*-Tol$_2$), 21.1 (s, *C*H$_3$), 21.0 (s, *C*H$_3$); ^{31}P{H^1}-NMR (162 MHz, C$_6$D$_6$, 25 °C): *δ* (ppm) 27.5 (d, $J_{P,P}$ = 38.3 Hz, 1P), 18.4 (b, 1P).

IR: 3,055 cm^{-1}, 2,954 cm^{-1}, 2,923 cm^{-1}, 2,853 cm^{-1}, 1,679 cm^{-1}, 1,435 cm^{-1}, 1,259 cm^{-1}, 1,094 cm^{-1}, 1,068 cm^{-1}, 1,028 cm^{-1}, 754 cm^{-1}, 691 cm^{-1}, 524 cm^{-1}.

Synthesis of self-hydrogenated complex (5)

[(^{Ph}bppe$^{H,CH^{p}Tol_2}$)Ni]$_2$(μ-N$_2$) (10 mg, 0.006 mmol) was weighed in a vial and dissolved in toluene (0.5 ml). A solution of diphenylacetylene (11 mg, 0.06 mmol) in toluene (0.5 ml) was immediately added and the solution was mixed. The solution was transferred to a J Young NMR tube. The tube was connected to a gas set-up and degassed by two freeze–pump–thaw cycles, and hydrogen gas was introduced to the solution inside of a Dewar with liquid nitrogen. The solution was warmed up at room temperature and placed in an oil bath at 70 °C for 16 h, after which the pressure was released and the solvent was evaporated. The solid was redissolved in a minimum amount of THF and precipitated with hexane. The precipitate was isolated by decantation, washed with cold hexane twice and dried to obtain an orange powder (8 mg, 70%). Suitable crystals for X-ray diffraction were obtained by vapour diffusion of hexane into a saturated toluene solution. The high sensitivity of the compound did not allow elemental analysis and high-resolution mass spectrometry data to be collected.

^{1}H-NMR (400 MHz, C$_6$D$_6$, 25 °C): *δ* (ppm) 8.52–8.38 (m, 1H, *p*-Tol$_2$CH–CH$_2$–C*H*), 7.80 (d, *J* = 7.6 Hz, 2H, Ar–*H*), 7.75 (t, *J* = 8.5 Hz, 2H, Ar–*H*), 7.37 (t, *J* = 7.5 Hz, 2H, Ar–*H*), 7.26 (t, *J* = 7.2 Hz, 1H, Ar–*H*), 7.22–7.17 (m, 4H, Ar–*H*), 7.15–7.06 (m, 5H, Ar–*H*), 7.06–6.99 (m, 3H, Ar–*H*), 6.95 (dd, *J* = 9.3, 5.5 Hz, 2H, Ar–*H*), 6.89 (dd, *J* = 10.6, 7.1 Hz, 2H, Ar–*H*), 6.82 (td, *J* = 7.6, 4.0 Hz, 5H, Ar–*H*), 6.76 (d, *J* = 7.7 Hz, 2H, Ar–*H*), 6.71 (t, *J* = 7.7 Hz, 2H, Ar–*H*), 6.63 (dt, *J* = 19.9, 7.4 Hz, 3H, Ar–*H*), 6.51 (q, *J* = 5.6 Hz, 3H, Ar–*H*), 6.43 (t, *J* = 7.5 Hz, 1H, Ar–*H*), 5.83 (d, *J* = 7.7 Hz, 2H, Ar–*H*), 5.78–5.64 (m, 2H, Ar–*H*), 4.19 (d, *J* = 11.3 Hz, 1H, *p*-Tol$_2$C*H*–CH$_2$–CH), 4.16–4.11 (m, 1H, PhC*H*=C), 4.02 (td, *J* = 10.0, 3.5 Hz, 1H, PhC*H*=C), 2.64 (q, *J* = 11.9 Hz, 1H, CH_2), 2.24 (s, 3H, CH_3), 2.03 (s, 3H, CH_3), 1.49 (d, *J* = 13.8 Hz, 1H, CH_2).

^{13}C{H^1}-NMR (101 MHz, C$_6$D$_6$, 25 °C): *δ* (ppm) 150.5 (d, *J* = 18.3 Hz, Ar), 149.0–148.8 (m, Ar), 148.8 (s, Ar), 144.1–143.8 (m, Ar), 143.5 (s, Ar), 142.8 (s, Ar), 138.3 (d, *J* = 9.5 Hz, Ar), 138.0 (d, *J* = 9.9 Hz, Ar), 137.1 (s, Ar), 136.7 (s, Ar), 136.3 (s, Ar), 136.2 (d, *J* = 1.9 Hz, Ar), 135.9 (s, Ar), 135.3 (d, *J* = 14.9 Hz, Ar), 135.0 (d, *J* = 5.3 Hz, Ar), 134.7 (d, *J* = 8.0 Hz, Ar), 134.5 (s, Ar), 134.4 (s, Ar), 134.2 (s, Ar), 133.5 (s, Ar), 133.1 (s, Ar), 133.0 (s, Ar), 132.9 (d, *J* = 5.4 Hz, Ar), 132.8 (s, Ar), 130.4 (s, Ar), 130.1 (d, *J* = 6.1 Hz, Ar), 129.4 (s, Ar), 129.1 (d, *J* = 6.0 Hz, Ar), 128.9 (d, *J* = 5.5 Hz, Ar),

128.7 (s, Ar), 128.6 (s, Ar), 128.5 (d, J = 4.9 Hz, Ar), 127.5 (d, J = 8.1 Hz, Ar), 127.1 (d, J = 7.0 Hz, Ar), 126.3 (s, Ar), 125.5 (s, Ar), 124.9 (s, Ar), 124.5 (d, J = 4.1 Hz, Ar), 123.5 (s, Ar), 122.3 (s, Ar), 65.9 (d, J = 16.9 Hz, Ph*C*H = C), 61.7 (d, J = 15.8 Hz, Ph*C*H=C), 51.6 (s, *p*-Tol_2CH−CH_2−CH), 43.8 (dd, J = 25.8, 12.7 Hz, *p*-Tol_2CH−CH_2−*C*H), 39.0 (s, CH_2), 21.1 (d, J = 2.3 Hz, CH_3), 20.9 (d, J = 1.9 Hz, CH_3).

$^{31}P\{H^1\}$-NMR (162 MHz, C_6D_6, 25 °C): δ (ppm) 20.16 (d, $J_{P\text{-}P}$ = 48 Hz), 17.36 (d, $J_{P\text{-}P}$ = 48 Hz).

IR: 3,055 cm^{-1}, 2,923 cm^{-1}, 2,854 cm^{-1}, 1,588 cm^{-1}, 1,510 cm^{-1}, 1,435 cm^{-1}, 1,262 cm^{-1}, 1,094 cm^{-1}, 1,067 cm^{-1}, 892 cm^{-1}, 805 cm^{-1}, 693 cm^{-1}, 523 cm^{-1}.

Data availability

The data supporting the findings of this study are provided in the Article and its Supplementary Information and are also available from the corresponding author on reasonable request. Further experimental details, spectra of compounds, crystallographic details and additional discussions of computational details are provided in the Supplementary Information. Coordinates of all computed structures (energy minima and transitions states) are provided in the .xyz format. CCDC 2236144 (compound **5**) contains the Supplementary Data for this paper. These data can be obtained free of charge from The Cambridge Crystallographic Data Centre via www.ccdc.cam.ac.uk/data_request/cif. Source Data are provided with this paper.

References

74. *Basics on Arrayed-NMR and Data Analysis* (Resources, accessed January 2023); https://resources.mestrelab.com/data-analysis/
75. Schreurs, A. M. M., Xian, X. & Kroon-Batenburg, L. M. J. EVAL15: a diffraction data integration method based on ab initio predicted profiles. *J. Appl. Crystallogr.* **43**, 70–82 (2010).
76. Krause, L., Herbst-Irmer, R., Sheldrick, G. M. & Stalke, D. Comparison of silver and molybdenum microfocus X-ray sources for single-crystal structure determination. *J. Appl. Crystallogr.* **48**, 3–10 (2015).
77. Sheldrick, G. M. SHELXT—integrated space-group and crystal-structure determination. *Acta Crystallogr. A* **71**, 3–8 (2015).
78. Sheldrick, G. M. Crystal structure refinement with SHELXL. *Acta Crystallogr. C* **71**, 3–8 (2015).
79. Spek, A. L. Structure validation in chemical crystallography. *Acta Crystallogr. D* **65**, 148–155 (2009).
80. Frisch, M. J. et al. *Gaussian 16* Revision C.01 (Gaussian, Inc., 2016).

Acknowledgements

This project has received funding from the European Research Council (ERC) under the European Union's Horizon 2020 research and innovation program (grant agreement no. 715060). The X-ray diffractometer has been financed by the Netherlands Organization for Scientific Research (NWO). This work made use of the Dutch national e-infrastructure with the support of the SURF Cooperative using grants no. EINF-1254 and EINF-3520. The funders had no role in study design, data collection and analysis, decision to publish or preparation of the manuscript. We thank P. M. Pérez-García for his assistance with the analysis of the catalysis results and helpful discussions. We thank G. van Koten, W. Hill Harman, D. L. J. Broere and A. A. Thevenon-Kozub for insightful discussions.

Author contributions

M.-E.M. initiated and supervised the project. M.L.G.S-P. performed the experiments and DFT calculations. M.L. oversaw the acquisition, solving and interpretation of X-ray diffraction of the crystal structure. M.L.G.S-P. and M.-E.M. wrote the manuscript with the contribution of M.L. All authors approved the final manuscript.

Competing interests

The authors declare no competing interests.

Additional information

Supplementary information The online version contains supplementary material available at https://doi.org/10.1038/s41557-023-01380-1.

Correspondence and requests for materials should be addressed to Marc-Etienne Moret.

Peer review information *Nature Chemistry* thanks Alison Edwards, Helene Gerard and Robin Perutz for their contribution to the peer review of this work.